

XMM-Newton observation of the eclipsing binary Algol *

Xue-Juan Yang^{1,2}, Fang-Jun Lu², Bernd Aschenbach³ and Li Chen⁴

¹ Faculty of Materials, Optoelectronics and Physics, Xiangtan University, Xiangtan 411105, China; xjyang@xtu.edu.cn

² Particle Astrophysics Center, Institute of High Energy Physics, Chinese Academy of Sciences, Beijing 100049, China

³ Max-Planck-Institut für Extraterrestrische Physik, 85741 Garching, Germany

⁴ Department of Astronomy, Beijing Normal University, Beijing 100875, China

Received 2010 July 18; accepted 2010 November 17

Abstract We present an *XMM-Newton* observation of the eclipsing binary Algol which contains an X-ray dark B8V primary and an X-ray bright K2IV secondary. The observation covered the optical secondary eclipse and captured an X-ray flare that was eclipsed by the B star. The *XMM-Newton* European Photon Imaging Camera and Reflection Grating Spectrometer spectra of Algol in its quiescent state are described by a two-temperature plasma model. The cool component has a temperature around 6.4×10^6 K while that of the hot component ranges from 2 to 4.0×10^7 K. Coronal abundances of C, N, O, Ne, Mg, Si and Fe were obtained for each component for both the quiescent and the flare phases, generally with upper limits for S and Ar, and upper limits for C, N, and O from the hot component. F-tests show that the abundances do not need to be different between the cool and the hot component and between the quiescent and the flare phase with the exception of Fe. Although the Fe abundance of the cool component remains constant at ~ 0.14 , the hot component shows an Fe abundance of ~ 0.28 , which increases to ~ 0.44 during the flare. This increase is expected from the chromospheric evaporation model. The absorbing column density N_H of the quiescent emission is 2.5×10^{20} cm⁻², while that of the flare-only emission is significantly lower and consistent with the column density of the interstellar medium. This observation substantiates earlier suggestions of the presence of X-ray absorbing material in the Algol system.

Key words: stars: abundance — star: binaries: eclipsing — stars: flare — stars: individual: Algol

1 INTRODUCTION

Algol (β Per) is a nearby eclipsing binary with an early main-sequence (B8V) primary and a cool subgiant (K2IV) secondary. This system is only 28.46 pc away (Hipparcos parallax measurements, ESA 1997) and has a period of about 2.87 d and an orbital inclination of 81° . The radii of the two companion stars (R_B and R_K) are 3.0 and $3.4 R_\odot$, respectively, and their separation is $14.14 R_\odot$ (Hill et al. 1971; Richards 1993). It is a semi-detached system with the K star filling its Roche lobe.

* Supported by the National Natural Science Foundation of China.

The mass transfer occurs in the form of gas streams from the K star to the B star which become an annulus around the B star (Richards 1993; Richards et al. 1995; Richards 2001; Richards 2004; Retter et al. 2005). Algol was first detected in X-rays by SAS 3 (Schnopper et al. 1976; Tomkin & Lambert 1978) and confirmed as a strong X-ray emitter by Harnden et al. (1977). It is generally accepted that the K star has an active corona which accounts for most of the X-ray flux of the system, whereas the B star is X-ray dark (White et al. 1980). This was proved for the first time by Chung et al. (2004) by the detection of Doppler shifts of the spectra caused by orbital motion of the K star. Given an active corona, flares typically appear every day with a duration of several to many hours.

Algol shows elemental abundances which differ from those of the Sun (Antunes et al. 1994; Schmitt & Ness 2004). Antunes et al. (1994) quoted abundances of Fe, O, Mg, Si, S, Ar and Ca which are lower than the solar photospheric values by a factor of 2–3, and values for N were quoted to be less than 0.1. With the exception of N, these results were generally confirmed by *Chandra* observations (Schmitt & Ness 2004). Schmitt & Ness (2002) studied a sample of late type stars including Algol and they found an enhancement of N. Drake (2003) also suggested that the N abundance is enhanced by a factor of 3, and C is depleted by a factor of 10 (both relative to HR1009, whose C/N abundance is consistent with that of the solar photosphere). These C and N abundances would lead to the conclusion that the K star has lost at least half of its initial mass.

The suggestion that flares have different elemental abundances has been confirmed from previous missions, such as *GINGA* (Stern et al. 1992), *ROSAT* (Ottmann & Schmitt 1996), *BeppoSAX* (Favata & Schmittl. 1999; Barban et al. 1999), *Chandra* (Nordon & Behar 2007) and *XMM-Newton* (Nordon & Behar 2008). They suggest that the elemental abundances of Algol's flaring region more closely resemble the photospheric than the quiescent coronal abundances, which might be a consequence of chromospheric evaporation (Güdel et al. 1999; Favata & Micela 2003 and references therein). At the beginning of the event, fresh chromospheric material evaporates in the flaring loop(s), and enhances the corona's elemental abundances; once the material has been transported to the flaring coronal structure, the fractionation mechanism, which is responsible for the lower abundance, would start operating, bringing the coronal abundance back to its quiescent value.

The absorbing column density (N_H) inferred from X-ray observations is usually higher than the column density of the interstellar medium (ISM) between Algol and the observer. Welsh et al. (1990) gave an upper limit of the ISM column density of $2.5 \times 10^{18} \text{ cm}^{-2}$ using the ISM NaI D line absorption of the B8 primary. Stern et al. (1995) derived a similar result from the He/H ratio using EUVE observations. The N_H derived from the *ROSAT* PSPC observation of Algol is about $5 \times 10^{19} \text{ cm}^{-2}$ (Ottmann 1994). Favata & Schmittl (1999) and Barban et al. (1999), using *BeppoSAX*, reported that N_H increased up to $> 10^{21} \text{ cm}^{-2}$ during the flare rise and decreased during the decay, which may possibly be associated with moving, cool material in the line of sight, e.g. a major coronal mass ejection.

In this paper, we present time resolved spectroscopy of Algol, using the *XMM-Newton* European Photon Imaging Camera (EPIC) and Reflection Grating Spectrometer (RGS) observations of Algol. Compared with the instruments used in earlier studies, the EPIC cameras are the first ones to have a combination of moderate spectral resolution, wide energy coverage, and high sensitivity, while RGS provides us with unparalleled sensitivity for high resolution spectroscopy in the soft X-ray band. These advantages permit us to perform a more detailed diagnosis of the plasma properties and their evolution as far as the corona of the K type secondary is concerned. The *XMM-Newton* observation covered the secondary eclipse and an X-ray flare was detected. Schmitt et al. (2003) presented a detailed study of the geometry of the flare, and we analyze the X-ray spectra of Algol in both the quiescent and flaring states. We can therefore study the mechanism of the X-ray emission of Algol in both the quiescent and the flaring states. In Section 2, we describe the observation and data reduction. The spectral properties of the overall and flare-only emissions are given in Section 3. The proposed local cool absorbing gas structures are discussed in Section 4 and a summary is provided in Section 5.

2 OBSERVATION AND DATA REDUCTION

Algol was observed with *XMM-Newton* on 2002–02–12 from 04:02:39 to 18:45:09 UTC. We use data from the EPIC-PN (Strüder et al. 2001), the (two) EPIC-MOS (Turner et al. 2001) detectors and the (two) RGS spectrometers (den Herder et al. 2001). The EPIC-PN was turned on at 04:42:18 and turned off at 18:34:45 UTC, with a net exposure time of about 50 ks, while the two EPIC-MOS and the two RGS detectors had a bit longer exposure, from 04:09:01 to 18:39:28 UTC and from 04:02:39 to 18:42:59, respectively. The EPIC-PN has an energy coverage of 0.15–15 keV, energy resolution of 80 eV at 1 keV, and a time resolution of 73 ms in the full-frame imaging mode in which the detector operated during this observation. The EPIC-MOS has a narrower energy coverage of 0.15–12 keV, a better energy resolution of 70 eV at 1 keV, and a time resolution of 2.6 s in the standard full-frame mode that was used in this observation. The RGS allows much better energy resolution measurements (i.e. 2.9 eV at 1 keV) in the soft X-ray range (0.3 to 2.1 keV). Algol was positioned at the target point, and thick filters were used in order to reduce the effect of strong optical loading of the CCD chips.

The X-ray data were analyzed using the XMMSAS software package. We found that there was no significant background flare and thus no time interval, except for the observation gaps, had to be eliminated from the dataset. Since Algol is very bright, the center part of the source was seriously affected by pile-up in the EPIC data, but not for the RGS data. Therefore, in the EPIC data analysis, we used the PN counts extracted from an annulus of 21.75 arcsec inner radius and 125 arcsec outer radius. For the MOS, inner and outer radii of 21.25 and 125 arcsec were taken for the selection annulus, respectively. According to the integrated PSFs of EPIC-PN and EPIC-MOS at 1.5 keV (which are near the peak of Algol's emission), photons in the chosen annuli make up about 10% of the total source photons for the EPIC-PN and EPIC-MOS detectors (Aschenbach et al. 2000). This factor was taken into account when we calculated the fluxes and emission measures.

The corresponding set of EPIC PN and MOS1 0.3 to 10 keV and the RGS1 0.3 to 2.1 keV background corrected light curves for the selected annuli and the entire observation are shown in Figure 1 with time bins of 100 s each. Using the ephemeris primary minimum = HJD 2,445,739.0030+2.^d8673285*E* (Al-Naimiy et al. 1985; Kim et al. 1989), the observation falls in the phase range 0.36–0.56 which includes the optical secondary eclipse.

In order to study the temporal evolution of the spectrum, we divided the observation into six segments and created a spectrum for each. The integration times were 5 000 to 10 000 s for these spectra. For the EPIC-PN, we only used the single events (PATTERN=0) for the spectral analysis, and the background was extracted from an annulus of 490 and 635 arcsec (the area contaminated by out-of-time events was excluded). For the two EPIC-MOS, we used both single and double events, and the background spectrum was extracted from an annulus of 490 and 660 arcsec. For the two RGS, only the first order data were used. Each spectrum was fitted with a two-temperature thermal plasma model (VMEKAL model; Mewe et al. 1995) in XSPEC. The free parameters are temperatures (T1, T2), emission measures (EM1, EM2) and abundances of C, N, O, Ne, Mg, Si, S, Ar and Fe for each of the two components. The abundances are in units of solar abundances given by Anders & Grevesse (1989). The WABS model (Morrison & McCammon 1983) was used to take care of interstellar photo-electric absorption. In the joint fit of the EPIC and RGS spectra, the RGS1, RGS2 and the EPIC emission measures were allowed to be different, because the EPIC counts were selected from a restricted annulus as described above, and the corresponding emission measures were of course much lower than those of the two RGS cases.

To study the properties of the flaring plasma, the flare period was cut into two sections, i.e. Sections 4 and 5 (c.f. Fig. 1). We chose the quiescent spectrum of the first 8000 s of the observation (c.f. Fig. 1) as the background spectrum, which is justified by the fact that the X-ray eclipse often starts around phase 0.40 (e.g., Schmitt & Favata 1999), corresponding to about 10 000 s after start of exposure of the present observation. Given that the quiescent emission dominates the RGS energy

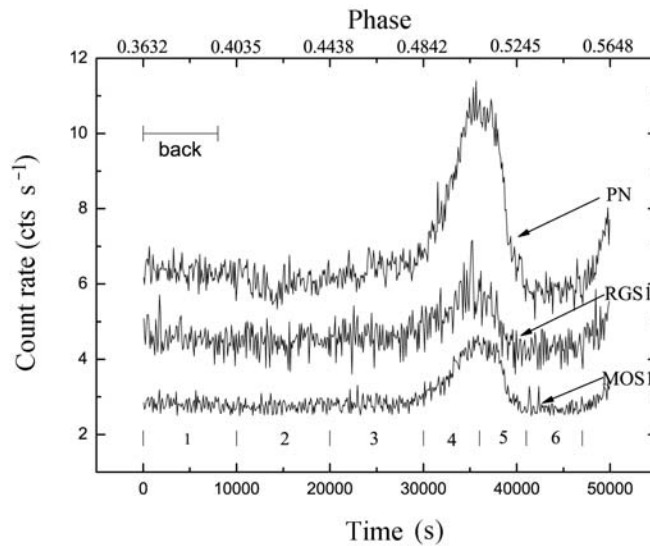


Fig. 1 EPIC PN and MOS1 0.3 to 10 keV and RGS1 0.3 to 2.1 keV light curves of Algol as a function of time and phase respectively, with time bins of 100 s. For clarity, the PN and MOS1 curves have each been moved up by 1 cts s⁻¹ and the RGS1 up by 2 cts s⁻¹. The horizontal line segment marked as “back” defines the time interval during which the background spectrum was taken for the analysis of the flare-only spectra.

band, use of the RGS data could not be made because of the fairly low signal to noise ratio. Taking into account that the quiescent emission was also eclipsed during the flare, we scaled the background spectrum by a factor of 0.9, which is the eclipsed fraction of the quiescent emission (Schmitt & Favata 1999). It should be noted that we assume that the quiescent emission arises from an isotropic corona of the K star and remains unchanged during the flare, and thus no rotation modulation was taken into account when we dealt with the background emission of the flare-only spectrum. The spectral analysis was performed with XSPEC. A one-temperature VMEKAL model in combination with the WABS model was used.

3 SPECTRA

3.1 The Spectra of the Overall X-ray Emission

The best-fit model parameters of the six spectra as well as their errors are listed in Tables 1 and 2 and are plotted in Figures 2, 3 and 4. The errors are calculated in XSPEC taking into account the full error projection, but they represent just the statistical errors at 90% confidence. As an example, Figure 5 shows the model fit to Spectrum #4.

From Tables 1 and 2 and Figures 2, 3 and 4, we derive the following results:

(1) The best-fit N_H values are about $\sim 2.5 \times 10^{20} \text{ cm}^{-2}$, and remain nearly constant during the entire observation. Considering that the potential effect of the EPIC cameras on the N_H values might be due to their low efficiency in the soft energy band, we also separately fit the EPIC and RGS data. The N_H value from the EPIC data is typically $1.6 \pm 0.5 \times 10^{20} \text{ cm}^{-2}$, while it is $3 \pm 0.4 \times 10^{20} \text{ cm}^{-2}$ from the RGS data. The results given in Table 1 and Figure 2 correspond to the weighted mean value of the two. Within the error bars, the N_H appears to be constant in time.

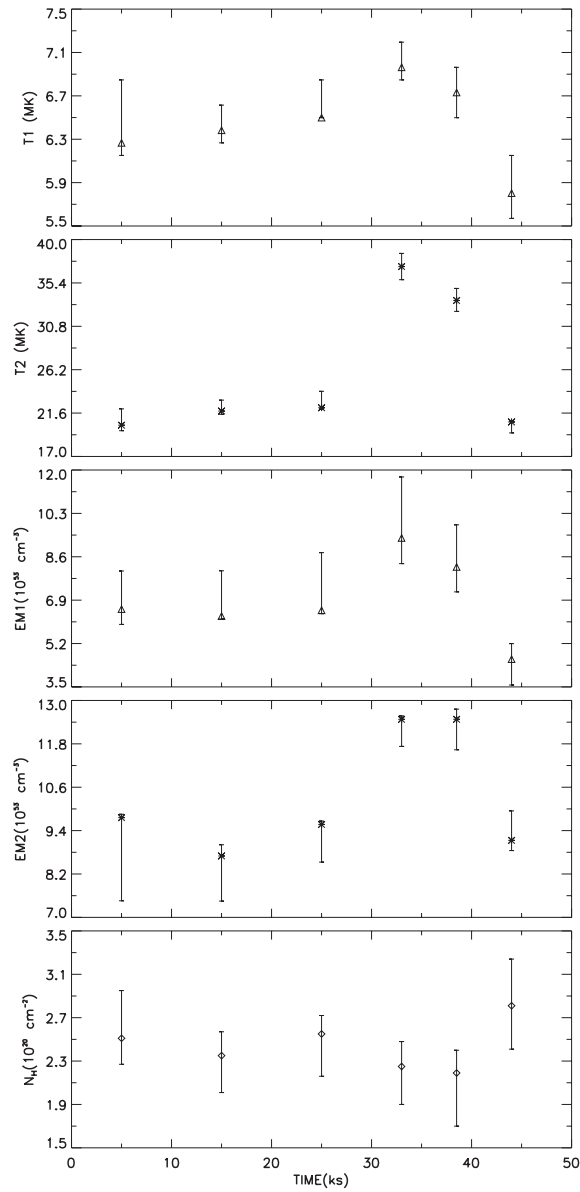


Fig. 2 Time distribution of the spectral parameters temperature (*top*), emission measure (*middle*) and column density for the cool component (index 1, “ \triangle ”) and hot component (index 2, “ $*$ ”). N_H , which is the same for the two components, is marked with “ \diamond ”.

This N_H is a factor of 100 higher than the upper limit of the ISM $\text{HI} + \text{H}_2$ column density towards Algol derived by Welsh et al. (1990). Fitting the spectra with N_H fixed at $2.5 \times 10^{18} \text{ cm}^{-2}$ yields significantly higher χ^2 values. With these two sets of N_H , χ^2 and degrees of freedom, we can carry out an F-test using the *ftest*-routine in XSPEC. The results show that most of the spectra have a probability of $< 0.01\%$ with N_H that small. An N_H value increase during the flare rise, which has been detected with BeppoSAX (Favata & Schmittl. (1999); Barban et al. 1999), has not

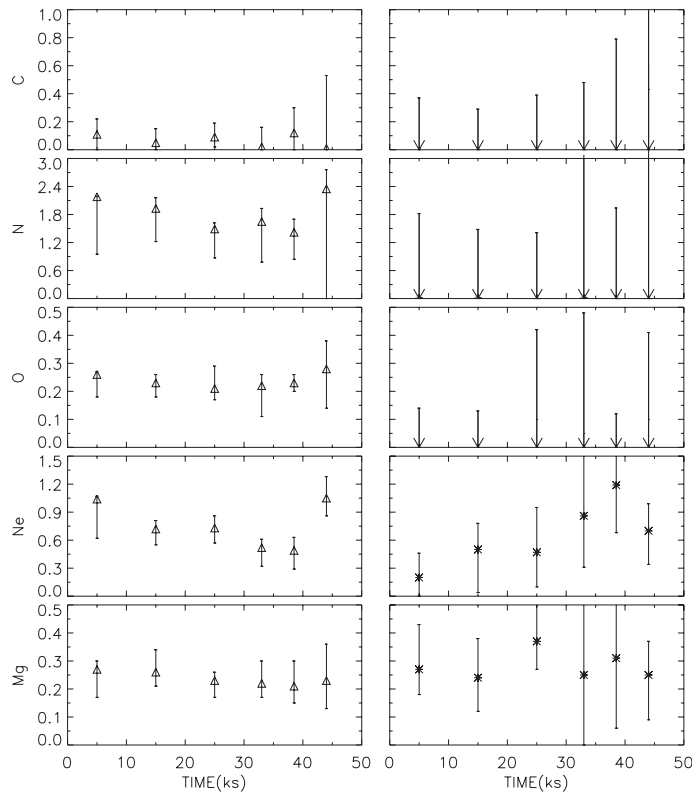


Fig. 3 Time distribution of the abundances of C, N, O, Ne, and Mg for the cool component (“△”) and hot component (“*”).

been detected in our observation, i.e., there is no evidence for major mass ejection during the flare to the extent that extra absorption occurs. We also tried to fit each of the two spectral components with different N_H values but the fit did not improve significantly, i.e., the N_H values of the two components show no significant difference.

(2) Both the temperature and the flux of the hot component show significant temporal variations similar to the light curve. This confirms the *ROSAT* PSPC results that the increase of the count rate during the flare is predominantly the result of an emission measure increase of the hot component (Ottmann 1994; Ottmann & Schmitt 1996).

(3) The RGS spectra are very similar to those from the *Chandra* LETGS (Ness et al. 2002). The emission lines of N, O, Ne, Mg and Fe are clearly visible as shown in Figure 5(b). The $Ly\alpha$ lines from MgXII (8.42 Å), Ne X(12.14 Å), OVIII(18.79 Å), and NVI(24.78 Å) can easily be recognized and have similar relative strengths as those in the LETGS spectra. One exception is that the Si emission lines are absent in the RGS spectra. We speculate that this is due to the low detecting efficiency of RGS around 6 Å. We note that the RGS spectra in the quiescent and flare state are very similar to each other. This is not surprising since the RGS spectra are dominated by the cool component, while most of the flare emission is from the hot component.

Table 3 demonstrates that the abundance pattern is generally compatible with that obtained from *ASCA* (Antunes et al. 1994) and *Chandra* observations (Schmitt & Ness 2004). An exception is observed for oxygen abundance of the hot component. However, oxygen, as well as carbon and

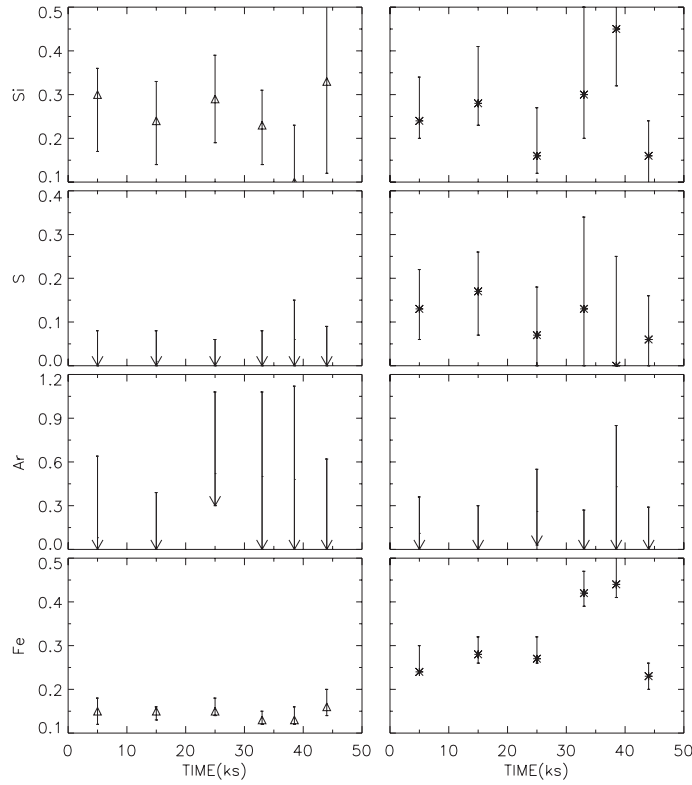


Fig. 4 Time distribution of the abundances of Si, S, Ar and Fe for the cool component (“△”) and hot component (“*”).

Table 1 Spectral Properties of Algol (2T VMEKAL Model)

No.	N_H ($\frac{10^{20}}{\text{cm}^2}$)	$T1$ (10^6 K)	EM1* ($\frac{10^{53}}{\text{cm}^3}$)	flux1† ($\frac{10^{-11} \text{erg}}{\text{cm}^2 \text{s}}$)	T2 (10^6 K)	EM2* ($\frac{10^{53}}{\text{cm}^3}$)	flux2† ($\frac{10^{-11} \text{erg}}{\text{cm}^2 \text{s}}$)	χ^2_{red}	DOF‡	F-test** probability
1	$2.51^{+0.44}_{-0.24}$	$6.27^{+0.58}_{-0.12}$	$6.55^{+1.49}_{-0.60}$	5.14	$20.31^{+1.74}_{-0.58}$	$9.76^{+0.09}_{-2.30}$	8.43	1.62	1979	3.28×10^{-4}
2	$2.35^{+0.22}_{-0.34}$	$6.38^{+0.23}_{-0.12}$	$6.28^{+1.77}_{-0.12}$	5.15	$21.82^{+1.16}_{-0.35}$	$8.70^{+0.31}_{-1.25}$	8.05	1.65	2000	9.26×10^{-5}
3	$2.55^{+0.17}_{-0.39}$	$6.50^{+0.35}_{-0.00}$	$6.50^{+2.26}_{-0.13}$	5.24	$22.17^{+1.74}_{-0.12}$	$9.57^{+0.09}_{-1.04}$	8.93	1.63	2051	9.50×10^{-4}
4	$2.25^{+0.23}_{-0.35}$	$6.96^{+0.23}_{-0.12}$	$9.34^{+2.39}_{-1.00}$	6.67	$37.14^{+1.39}_{-1.39}$	$12.48^{+0.09}_{-0.75}$	16.1	1.53	1326	1.30×10^{-13}
5	$2.19^{+0.21}_{-0.49}$	$6.73^{+0.23}_{-0.23}$	$8.20^{+1.65}_{-0.98}$	5.89	$33.54^{+1.28}_{-1.16}$	$12.48^{+0.28}_{-0.84}$	15.5	1.50	1136	2.14×10^{-7}
6	$2.81^{+0.43}_{-0.40}$	$5.80^{+0.35}_{-0.23}$	$4.59^{+0.61}_{-1.01}$	4.49	$20.66^{+0.12}_{-1.16}$	$9.13^{+0.82}_{-0.28}$	8.18	1.71	957	4.29×10^{-2}

* EPIC emission measure;

** F-test probability for adopting identical abundances for the two components;

† unabsorbed EPIC energy flux in the range of 0.5–10 keV;

‡ degrees of freedom.

nitrogen, should be fully ionized at these high temperatures so that emission lines cannot reliably be used to constrain abundances, which means that in our case the abundances are poorly determined. The relatively high N abundance and N/C ratio (for the cool component), which have been detected earlier by Schmitt & Ness (2002), Drake (2003) and Schmitt & Ness (2004), are clearly present

Table 2 Spectral Properties of Algol (2T VMEKAL Model)

No.	C	N	O	Ne	Mg	Si	S	Ar	Fe
1	0.11 ^{+0.11} _{-0.11}	2.18 ^{+0.01} _{-1.23}	0.26 ^{+0.01} _{-0.08}	1.04 ^{+0.03} _{-0.42}	0.27 ^{+0.03} _{-0.10}	0.30 ^{+0.06} _{-0.13}	< 0.08	< 0.64	0.15 ^{+0.03} _{-0.03}
2	0.05 ^{+0.10} _{-0.05}	1.93 ^{+0.23} _{-0.71}	0.23 ^{+0.03} _{-0.05}	0.72 ^{+0.09} _{-0.17}	0.26 ^{+0.08} _{-0.05}	0.24 ^{+0.09} _{-0.10}	< 0.08	< 0.39	0.15 ^{+0.01} _{-0.02}
3	0.09 ^{+0.10} _{-0.07}	1.49 ^{+0.13} _{-0.62}	0.21 ^{+0.08} _{-0.04}	0.73 ^{+0.13} _{-0.16}	0.23 ^{+0.03} _{-0.06}	0.29 ^{+0.10} _{-0.10}	< 0.06	< 1.08	0.15 ^{+0.03} _{-0.01}
4	0.02 ^{+0.14} _{-0.02}	1.65 ^{+0.28} _{-0.87}	0.22 ^{+0.04} _{-0.11}	0.52 ^{+0.09} _{-0.20}	0.22 ^{+0.08} _{-0.05}	0.23 ^{+0.08} _{-0.09}	< 0.08	< 1.08	0.13 ^{+0.02} _{-0.01}
5	0.12 ^{+0.18} _{-0.12}	1.42 ^{+0.28} _{-0.58}	0.23 ^{+0.03} _{-0.03}	0.49 ^{+0.14} _{-0.20}	0.21 ^{+0.09} _{-0.06}	0.10 ^{+0.13} _{-0.10}	< 0.15	< 1.12	0.13 ^{+0.03} _{-0.01}
6	0.01 ^{+0.52} _{-0.01}	2.35 ^{+0.41} _{-2.35}	0.28 ^{+0.10} _{-0.14}	1.05 ^{+0.23} _{-0.19}	0.23 ^{+0.13} _{-0.10}	0.33 ^{+0.25} _{-0.21}	< 0.09	< 0.62	0.16 ^{+0.04} _{-0.02}
1	< 0.37	< 1.82	< 0.14	0.20 ^{+0.26} _{-0.20}	0.27 ^{+0.16} _{-0.09}	0.24 ^{+0.10} _{-0.04}	< 0.22	< 0.36	0.24 ^{+0.06} _{-0.00}
2	< 0.29	< 1.48	< 0.13	0.50 ^{+0.28} _{-0.46}	0.24 ^{+0.14} _{-0.12}	0.28 ^{+0.13} _{-0.05}	< 0.26	< 0.30	0.28 ^{+0.04} _{-0.02}
3	< 0.39	< 1.41	< 0.42	0.47 ^{+0.48} _{-0.37}	0.37 ^{+0.22} _{-0.10}	0.16 ^{+0.11} _{-0.04}	< 0.18	< 0.55	0.27 ^{+0.05} _{-0.01}
4	< 0.48	< 3.08	< 0.48	0.86 ^{+0.78} _{-0.55}	0.25 ^{+0.30} _{-0.25}	0.30 ^{+0.20} _{-0.10}	< 0.34	< 0.27	0.42 ^{+0.05} _{-0.03}
5	< 0.79	< 1.94	< 0.12	1.19 ^{+0.82} _{-0.51}	0.31 ^{+0.27} _{-0.25}	0.45 ^{+0.23} _{-0.13}	< 0.25	< 0.85	0.44 ^{+0.06} _{-0.03}
6	< 1.00	< 5.02	< 0.41	0.70 ^{+0.29} _{-0.36}	0.25 ^{+0.12} _{-0.16}	0.16 ^{+0.08} _{-0.09}	< 0.16	< 0.29	0.23 ^{+0.03} _{-0.03}

Notes: The top six rows are for the *cool* component and the lower six rows are for the *hot* component.

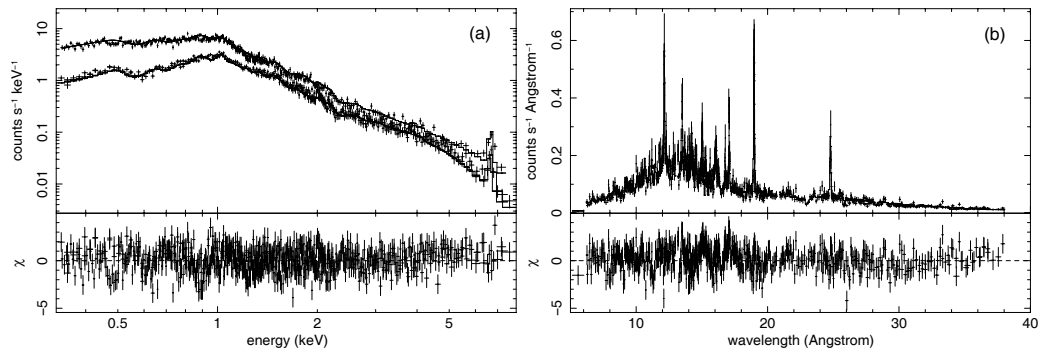


Fig. 5 Two-temperature thermal plasma model fits to Spectrum #4. Panel (a) is for EPIC, where the top curve is for the PN and the bottom curve is for MOS1 and MOS2, while Panel (b) is for RGS1 and RGS2. The x -axis for RGS is wavelength instead of energy and the y -axis is not plotted in log scale, to make it more easy to recognize the emission lines. The EPIC spectra show the presence of an Fe 6.7 keV line.

in our observation as well. They therefore support the suggestion made in the papers quoted above that the N enhancement is related to the CNO-cycle operating in the core of the star. Furthermore, the active corona of Algol seems to be Fe-poor, which has been suggested before by Antunes et al. (1994) and Stern et al. (1995). Iron is likely to be depleted in the corona (Drake 2003).

Comparing the abundances of the cool and the hot component (c.f. Table 2, Figs. 3 and 4), we note that, apart from perhaps the light elements C, N, and O, there appear to be no significant differences for Ne, Mg and Si. Because of the large uncertainties, the abundances of S and Ar are also not really accessible, but upper limits can be provided. A clear difference, however, exists for Fe (c.f. Fig. 6). In fact, F-tests show that we cannot rule out the case where the abundances of the cool and the hot component are identical, with the exception of Fe. Figure 6 shows the best-fit and the corresponding error contours for the Fe abundances of the cool and hot component of Spectrum #1, i.e. during the quiescent phase. Up to the 4σ level, the abundances differ from each other. For the best

Table 3 Comparison of coronal elemental abundances from *XMM-Newton* (this paper), *ASCA* (Antunes et al. 1994) and *Chandra LETGS* (Schmitt & Ness 2004).

Element	This paper* Cool plasma	This paper* Hot plasma	Antunes et al. Low State	Antunes et al. Medium State	Antunes et al. High State	Schmitt & Ness
C	$0.07^{+0.10}_{-0.03}$	$0.08^{+0.20}_{-0.07}$	<i>n.a.</i>	<i>n.a.</i>	<i>n.a.</i>	< 0.04
N	$1.84^{+0.10}_{-0.50}$	$0.01^{+1.28}_{-0.00}$	< 0.1	< 0.1	< 0.1	2.00
O	$0.24^{+0.02}_{-0.03}$	$0.04^{+0.11}_{-0.02}$	$0.30^{+0.04}_{-0.04}$	$0.31^{+0.03}_{-0.03}$	$0.24^{+0.03}_{-0.03}$	0.25
Ne	$0.76^{+0.10}_{-0.05}$	$0.65^{+0.22}_{-0.17}$	$0.76^{+0.10}_{-0.10}$	$1.22^{+0.08}_{-0.08}$	$1.08^{+0.08}_{-0.08}$	0.95
Mg	$0.24^{+0.03}_{-0.03}$	$0.28^{+0.09}_{-0.07}$	$0.48^{+0.06}_{-0.06}$	$0.64^{+0.05}_{-0.05}$	$0.47^{+0.04}_{-0.04}$	0.50
Si	$0.25^{+0.05}_{-0.05}$	$0.27^{+0.09}_{-0.07}$	$0.43^{+0.05}_{-0.05}$	$0.65^{+0.05}_{-0.04}$	$0.47^{+0.03}_{-0.03}$	0.45
S	$0.01^{+0.03}_{-0.01}$	$0.09^{+0.06}_{-0.03}$	$0.29^{+0.07}_{-0.07}$	$0.21^{+0.05}_{-0.05}$	$0.09^{+0.04}_{-0.04}$	<i>n.a.</i>
Ar	$0.26^{+0.23}_{-0.12}$	$0.14^{+0.12}_{-0.08}$	$0.10^{+0.10}_{-0.10}$	$0.14^{+0.12}_{-0.12}$	$0.10^{+0.11}_{-0.11}$	<i>n.a.</i>
Fe	$0.14^{+0.01}_{-0.01}$	$0.31^{+0.02}_{-0.01}$	$0.30^{+0.01}_{-0.01}$	$0.37^{+0.02}_{-0.02}$	$0.32^{+0.01}_{-0.01}$	0.20

Notes: * Average of best-fit values of the six spectra.

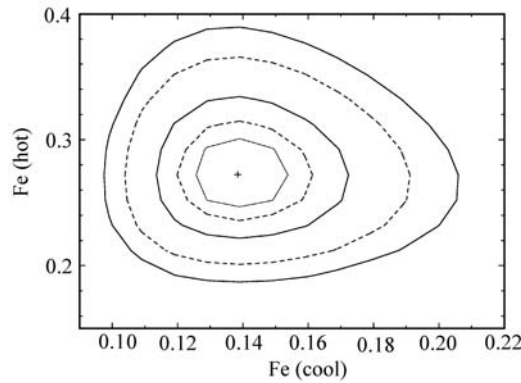


Fig. 6 Fe abundance of the hot component versus the Fe abundance of the cool component obtained from Spectrum #1 of the quiescent phase. The best-fit value is marked by a cross; the contours correspond to 1σ to 5σ errors in increments of 1σ .

fit, the abundances are $\text{Fe}(\text{cool}) \sim 0.14$ and $\text{Fe}(\text{hot}) \sim 0.28$. This result holds not only for Spectrum #1 but for the entire quiescent phase, including the post-flare phase covered by Spectrum #6. From the *ROSAT* PSPC observation (Ottmann 1994), it was concluded that the low and high temperature components are rather co-spatial with respect to the stellar surface. We therefore speculate that the cool and hot components might come from different layers or that the hot regions are much smaller in size than the radius of the K star.

We admit that the two components are not likely to represent physically distinct temperatures. A temperature gradient in the corona might exist, or the two temperatures are just a short-cut expression of a temperature dependent emission measure. In order to check whether the different abundances of the cool and hot components we obtained above are real or only the consequence of an oversimplified temperature model, we also fit the spectra with a three-temperature VMEKAL model. Similar to what we have done in the two-temperature VMEKAL model fitting, we first set the three iron abundances as free parameters and then make the three components share the same iron abundance. The fitting results are given in Table 4. The F-test shows that for Spectra #1–#5, the probabilities that the three components have the same abundance are lower than 5×10^{-5} , similar to those of

Table 4 Main Spectral Properties of Algol (3T VMEKAL Model)

No.	$T1$	$T2$	$T3$	Fe			χ_{red}^2	DOF*	F-test† probability
	(10^6 K)	(10^6 K)	(10^6 K)	Fe1	Fe2	Fe3			
1	$4.76^{+0.23}_{-0.35}$	$8.24^{+0.58}_{-0.46}$	$23.91^{+1.16}_{-1.04}$	$0.17^{+0.04}_{-0.02}$	$0.18^{+0.06}_{-0.03}$	$0.31^{+0.04}_{-0.04}$	1.45	1982	
2	$4.76^{+0.23}_{-0.35}$	$8.24^{+0.58}_{-0.35}$	$25.53^{+1.39}_{-1.28}$	$0.17^{+0.05}_{-0.03}$	$0.18^{+0.06}_{-0.04}$	$0.35^{+0.05}_{-0.04}$	1.50	2003	
3	$4.64^{+0.23}_{-0.35}$	$8.12^{+0.46}_{-0.35}$	$26.92^{+1.39}_{-1.28}$	$0.25^{+0.12}_{-0.06}$	$0.15^{+0.03}_{-0.03}$	$0.36^{+0.04}_{-0.05}$	1.44	2054	
4	$4.99^{+0.23}_{-0.35}$	$9.40^{+0.70}_{-0.93}$	$40.39^{+2.79}_{-2.09}$	$0.15^{+0.04}_{-0.02}$	$0.22^{+0.09}_{-0.07}$	$0.41^{+0.05}_{-0.06}$	1.37	1329	
5	$4.99^{+0.35}_{-0.93}$	$9.05^{+0.70}_{-1.28}$	$34.93^{+2.79}_{-1.04}$	$0.17^{+0.14}_{-0.03}$	$0.22^{+0.12}_{-0.09}$	$0.45^{+0.07}_{-0.06}$	1.36	1139	
6	$4.76^{+0.35}_{-0.12}$	$8.36^{+1.16}_{-0.23}$	$23.09^{+0.81}_{-1.97}$	$0.20^{+0.02}_{-0.05}$	$0.27^{+1.05}_{-0.03}$	$0.26^{+0.02}_{-0.08}$	1.52	960	
1	$4.87^{+0.23}_{-0.35}$	$8.36^{+0.35}_{-0.35}$	$22.63^{+0.81}_{-0.93}$		$0.22^{+0.02}_{-0.02}$		1.47	1984	5.12×10^{-5}
2	$4.99^{+0.12}_{-0.35}$	$8.59^{+0.35}_{-0.46}$	$23.56^{+1.04}_{-0.93}$		$0.23^{+0.03}_{-0.02}$		1.52	2005	3.43×10^{-8}
3	$4.99^{+0.23}_{-0.23}$	$8.82^{+0.46}_{-0.23}$	$24.60^{+1.39}_{-1.04}$		$0.24^{+0.02}_{-0.02}$		1.47	2056	2.29×10^{-5}
4	$5.22^{+0.35}_{-0.12}$	$9.75^{+0.70}_{-0.23}$	$40.39^{+5.45}_{-1.28}$		$0.26^{+0.02}_{-0.05}$		1.40	1331	1.98×10^{-7}
5	$5.34^{+0.23}_{-0.35}$	$9.52^{+0.46}_{-0.70}$	$34.23^{+2.32}_{-1.86}$		$0.31^{+0.05}_{-0.05}$		1.39	1141	5.53×10^{-7}
6	$4.64^{+0.35}_{-0.35}$	$8.24^{+0.35}_{-0.46}$	$23.09^{+1.04}_{-0.93}$		$0.24^{+0.03}_{-0.03}$		1.52	962	3.60×10^{-1}

* degrees of freedom.

† F-test probability for adopting identical iron abundance for the three components.

the two-temperature model fitting. The only exception is Spectrum #6, for which the corresponding probability is 0.36; one possible reason is that Spectrum #6 contains fewer counts than the other spectra. In Figure 7, as an example, we show the comparison of the three-temperature spectral fittings to Spectrum #5, with the three iron abundances equal to or different from each other. The apparent residual bump around 6.7 keV in the left panel also implies that the hot component has a higher iron abundance.

(4) The abundance of Fe and possibly the abundances of Ne and Si of the hot component appear to change during the flare (c.f. Table 2). The Fe abundance increased from 0.25 times the solar value in the quiescent state to about 0.5 during the flare. To put this in a more quantitative context, we carried out an F-test and assessed whether the elemental abundances were identical for the quiescent and the flare-only emission. This hypothesis can indeed be accepted but only if the abundances of Fe between the hot components differ. The cool component is consistent with one set of Fe abundance values for the quiescent and the flare-only phase.

Figure 8 shows the best fit and the error contours for the Fe abundance of the hot versus the cool component for a flare spectrum. The Fe-abundances are inconsistent with each other well beyond the 5σ level. Whereas the Fe abundance of the cool component stays ~ 0.14 , the best fit for the Fe abundance of the hot component is now ~ 0.44 , which means an increase by a factor of ~ 1.6 between the quiescent and the flare phase occurred. This kind of behavior of the Fe abundance still holds for the three-temperature model, i.e., the Fe abundances for the cool and middle component remain unchanged, while that of the hot component increases during the flare, although not as much as that in the two-temperature model. This kind of increase for Fe abundance during the flare has also been detected in CN Leonis (Liefke et al. 2010).

This Fe abundance increase during a flare may be attributed to chromospheric evaporation (Favata & Micela 2003). The abundances of Ne and Si for the hot component may show a similar behavior, although with much larger uncertainty. This could further support the idea of chromospheric evaporation. The elemental abundances of the cool component remain nearly unchanged during the entire observation, which represent additional support for the hot component dominating the flare.

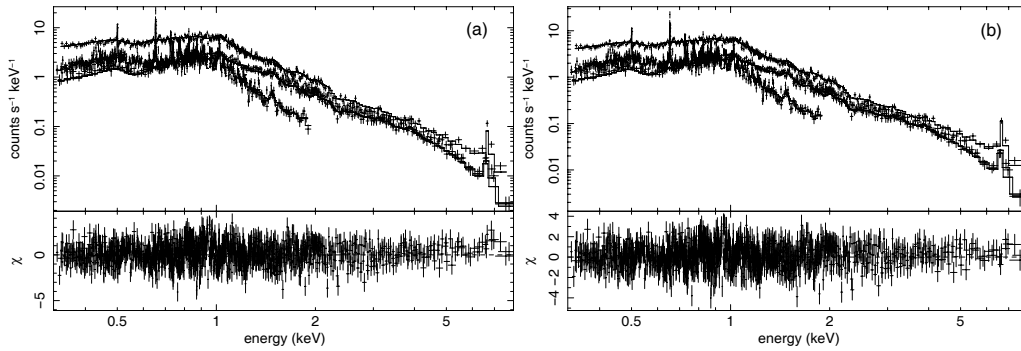


Fig. 7 Three-temperature thermal plasma model fits to Spectrum #5. Panel (a) displays global abundances of all the elements for the three component case, while Panel (b) displays only Fe in the relaxed case.

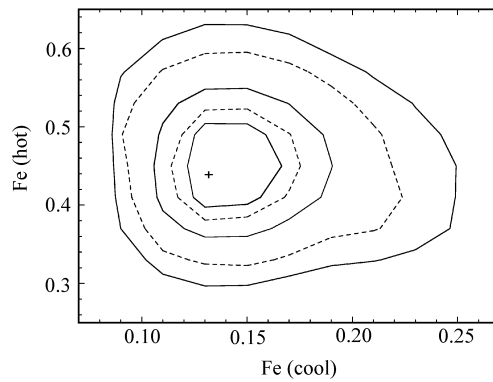


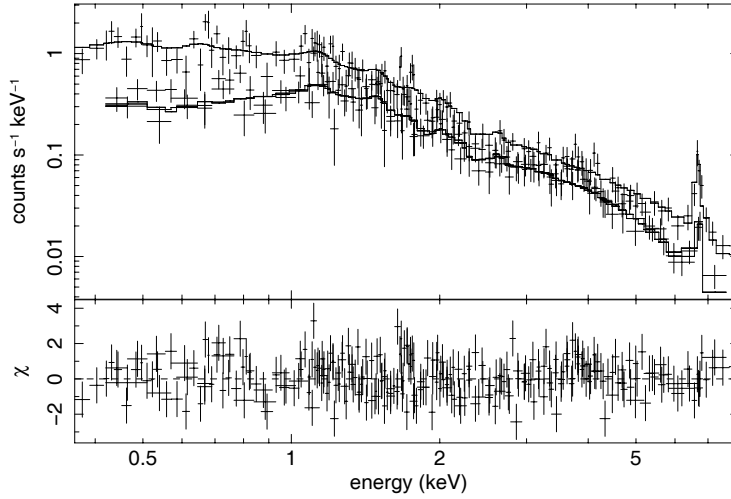
Fig. 8 Fe abundance of the hot component versus the Fe abundance of the cool component obtained from Spectrum #5 of the flare phase. The best-fit value is marked by a cross; the contours correspond to 1σ to 5σ errors in increments of 1σ .

3.2 The Flare-only Spectra

The spectra of the flare-only emission can be well fitted with a one-temperature VMEKAL model. Table 5 gives the fitted parameters and Figure 9 shows the model fit to the flare-only Spectrum #2 (corresponding to the overall Spectrum #5). The temperature of the flare emission is around 6.2×10^7 K and it shows no detectable variations during the flare. Obviously, the flare temperature is much higher than the temperature of the hot component of the quiescent state. The elemental abundances are comparable to those of the hot component and they show no variation either (see Table 4). The best-fit N_H of the flare emission is consistent with no absorption at all for each of the two spectra. Taking into account the uncertainties, it is still significantly lower than the N_H values associated with the quiescent emission, which is consistent with the results of the *ROSAT* observation (Ottmann 1994; Ottmann & Schmitt 1996). We then used the F-test to examine whether the N_H difference between the flare emission and the quiescent emission is real or just a statistical fluctuation. This test is based on the comparison of the χ^2 values and the degrees of freedom

Table 5 Best Fit Results for Flare-only Spectra

No.	t (s)	N_H $(\frac{10^{20}}{\text{cm}^2})$	T (10^6 K)	Z (Z_\odot)	EM $(\frac{10^{53}}{\text{cm}^3})$	flux $(\frac{10^{-11} \text{erg}}{\text{cm}^2 \text{s}})$	χ_{red}^2	DOF	F-test probability
1	6000	$< 0.60(2\sigma)$	$63.6^{+4.4}_{-4.8}$	$0.55^{+0.12}_{-0.12}$	$5.33^{+0.21}_{-0.15}$	9.24	1.11	373	9.50×10^{-6}
2	5000	$< 1.58(2\sigma)$	$60.1^{+4.1}_{-5.4}$	$0.64^{+0.16}_{-0.15}$	$4.56^{+0.25}_{-0.23}$	7.94	1.02	264	5.71×10^{-3}

**Fig. 9** Flare-only case of Spectrum #2. The upper curve is for the PN and the lower curve is for MOS1 and MOS2.

of the model fits to the flare-only spectra with N_H as a free parameter against N_H being fixed to the mean N_H of the quiescent emission ($2.5 \times 10^{20} \text{ cm}^{-2}$). As shown by the values listed in Table 4, the N_H of the flare emission is lower than that of the quiescent emission at a significance level greater than 99.5%. A similar behavior is suggested by the *ROSAT* observation with an overall N_H of about $5 \times 10^{19} \text{ cm}^{-2}$ (Ottmann 1994), while the flare-only N_H is around $1 \times 10^{19} \text{ cm}^{-2}$ (Ottmann & Schmitt 1996).

In order to check whether the above results are intrinsic properties of the flare-only emission or are related to the particular model for the background spectrum, we also tried the quiescent spectrum in time interval 2 as the background spectrum to create the flare-only spectra. These spectra are fitted with the same VMEKAL model, and the results are very consistent with the previously obtained ones. In fact, this is not surprising given that the parameters of the overall Spectra #1 and #2 are consistent with each other within the error bars. We therefore conclude that values for the low absorption column density, the high temperature and the high metallicity of the flare-only emission are robust.

4 COOL ABSORBING GAS SURROUNDING THE K STAR

The mean N_H value of the quiescent emission derived in this paper is about $2.5 \times 10^{20} \text{ cm}^{-2}$, which is at least two orders of magnitude higher than the interstellar $\text{HI} + \text{H}_2$ column density reported by Welsh et al. (1990). The low energy calibration of *XMM* may affect our results, but not as

much as two orders of magnitude as stated in Section 3.1. Stern et al. (1995) estimated N_H to be $2 \times 10^{18} \text{ cm}^{-2}$ using an EUVE observation, which is consistent with that of Welsh et al. (1990). In addition, N_H of $5 \times 10^{19} \text{ cm}^{-2}$ obtained in the ROSAT PSPC observation is lower than our result (Ottmann 1994), but still 20 times higher than the ISM column density. However, since Welsh et al. (1990) inferred the ISM column density using the Na line absorption by the continuum of the B type primary that is X-ray dark, and since the N_H values obtained in X-ray observations correspond to the absorbing column densities of the X-ray emitting K type secondary, the higher N_H values thus imply that there exists cool gas just surrounding the K star. Furthermore, the result of Stern et al. (1995) was based on the He/H ratio, without an ionized He. This would be the case for our model of ionized local absorbing material, which would make the material transparent to EUV but not to X-rays. Because no orbital (and so rotational) modulation of N_H has been detected by either ROSAT (Ottmann 1994) or XMM-Newton, the cool gas should be distributed quite homogeneously relative to the longitude of the K star's surface. The N_H difference between the ROSAT and XMM-Newton observations might further suggest that the amount of cool gas surrounding the K star changes over the long term.

The location and configuration of this cold matter is unclear. However, in the framework of the two polar lobe model (Favata et al. 2000; Retter et al. 2005; Peterson et al. 2010) for the site of the quiescent corona, one could imagine that the absorption column density is highest in or around those lobes, where the quiescent corona dominates. It is reduced towards the equatorial regions, at which location the certainly non-polar flare of this XMM-Newton observation is located.

Such a configuration would also explain the observation of the 133 Å line. In the polar regions, i.e. the lobes, it is likely to be completely absorbed, but it would become observable if only a small fraction of coronal emission would also exist in sub-polar regions of low absorption. The corona stretching down from the polar regions has been shown by Schmitt et al. (2003) in discussing the location of the quiescent coronal emission of just these XMM-Newton observations.

5 SUMMARY

We have analyzed an XMM-Newton observation of the eclipsing binary Algol, in which the interval of the secondary optical minimum and some preceding section in the orbit were covered. During the eclipse of the X-ray bright K star, a flare occurred so that we can study both the quiescent corona and an eclipsed flare. We combined the data of all four X-ray instruments onboard XMM-Newton, which give spectral data at high resolution with the RGSs from 0.3 – 2 keV and medium resolution data with the EPIC cameras from 0.3 – 10 keV.

Satisfactory fits have been obtained over the entire energy band using the two-temperature VMEKAL model for the overall spectrum. We cannot rule out that the elemental abundances of the spectrum's low temperature and high temperature components are identical, but the abundance of Fe is clearly different at the 4σ level for the quiescent phase and significantly more than 5σ for the flare phase, indicating that the high temperature and low temperature plasma components are not well mixed. We also observed a significant Fe abundance increase in the hot component by a factor of ~ 1.6 during the flare, which supports the idea of chromospheric evaporation.

The fits to the N_H column density reveal values around $2.5 \times 10^{20} \text{ cm}^{-2}$ for the quiescent corona which are far in excess of the interstellar column density. On the other hand, the fits to the flare-only emission are consistent with no absorption exceeding the interstellar value. We propose that the line of sight column density across Algol is not uniform. It is sufficiently high towards the polar regions, and reduces towards the equatorial regions.

Acknowledgements We thank the anonymous referee for the very helpful comments. This project is supported by the National Natural Science Foundation of China (Grant Nos. 10903007, 10778716 and 10878012). This work is based on observations with XMM-Newton, an ESA science mission with instruments and contributions directly funded by ESA member states and the USA (NASA).

References

- Al-Naimiy, H. M. K., Mutter, A. A. A., & Flaih, H. A. 1985, *Ap&SS*, 108, 227
- Anders, E., & Grevesse, N. 1989, *Geochim. Cosmochim. Acta*, 53, 197
- Antunes, A., Nagase, F., & White, N. E. 1994, *ApJ*, 436, L83
- Aschenbach, B., Briel, U. G., Haberl, F., Braeuninger, H. W., Burkert, W., Oppitz, A., Gondoin, P., & Lumb, D. H. 2000, *Proc. SPIE*, 4012, 731
- Barban, C., Michel, E., Martic, M., Schmitt, J., Lebrun, J. C., Baglin, A., & Bertaux, J. L. 1999, *A&A*, 350, 617
- Chung, S. M., Drake, J. J., Kashyap, V. L., Lin, L. W., & Ratzlaff, P. W. 2004, *ApJ*, 606, 1184
- den Herder, J. W., et al. 2001, *A&A*, 365, L7
- Drake, J. J. 2003, *ApJ*, 594, 496
- Favata, F., Micela, G., Reale, F., Sciortino, S., & Schmitt, J. H. M. M. 2000, *A&A*, 362, 628
- Favata, F., & Micela, G. 2003, *Space Sci. Rev.*, 108, 577
- Favata, F., & Schmitt, J. H. M. M. 1999, *A&A*, 350, 900
- Güdel, M., Linsky, J. L., Brown, A., & Nagase, F. 1999, *ApJ*, 511, 405
- Harnden, F. R., Jr., Fabricant, D., Topka, K., Flannery, B. P., Tucker, W. H., & Gorenstein, P. 1977, *ApJ*, 214, 418
- Hill, G., Barnes, J. V., Hutchings, J. B., & Pearce, J. A. 1971, *ApJ*, 168, 443
- Kim, H.-I. 1989, *ApJ*, 342, 1061
- Liefke, C., Fuhrmeister, B., & Schmitt, J. H. M. M. 2010, *A&A*, 514, A94
- Mewe, R., Kaastra, J. S., & Liedahl, D.A. 1995, *Legacy*, 6, 16
- Morrison, R., & McCammon, D. 1983, *ApJ*, 270, 119
- Ness, J.-U., Schmitt, J. H. M. M., Burwitz, V., Mewe, R., & Predehl, P. 2002, *A&A*, 387, 1032
- Nordon, R., & Behar, E. 2007, *A&A*, 464, 309
- Nordon, R., & Behar, E. 2008, *A&A*, 482, 639
- Ottmann, R. 1994, *A&A*, 286, L27
- Ottmann, R., & Schmitt, J. H. M. M. 1996, *A&A*, 307, 813
- Peterson, W. M., Mutel, R. L., Güdel, M., & Goss, W. M. 2010, *Nature*, 463, 207
- Retter, A., Richards, M. T., & Wu, K. 2005, *ApJ*, 621, 417
- Richards, M. T. 1993, *ApJS*, 86, 255
- Richards, M. T., et al. 1995, *ApJ*, 438, L103
- Richards, M. T. 2001, *Astromotography, Indirect Imaging Methods in Observational Astronomy*, 573, 276
- Richards, M. T. 2004, *Astronomische Nachrichten*, 325, 229
- Schmitt, J. H. M. M., & Ness, J.-U. 2002, *A&A*, 388, L13
- Schmitt, J. H. M. M., Ness, J.-U., & Franco, G. 2003, *A&A*, 412, 849
- Schmitt, J. H. M. M., & Ness, J.-U. 2004, *A&A*, 415, 1099
- Schnopper, H. W., et al. 1976, 210, L75
- Stern, R. A., Uchida, Y., Tsuneta, S., & Nagase, F. 1992, *ApJ*, 400, 321
- Stern, R. A., Lemen, J. R., Schmitt, J. H. M. M., & Pye, J. P. 1995, *ApJ*, 444, L45
- Strüder, L., et al. 2001, *A&A*, 365, L18
- Tomkin, J., & Lambert, D. L. 1978, *ApJ*, 222, L119
- Turner, M. J. L., et al. 2001, *A&A*, 365, L27
- Welsh, B. Y., Vedder, P. W., & Vallergera, J. V. 1990, *ApJ*, 358, 473
- White, N. E., Becker, R. H., Holt, S. S., Boldt, E. A., & Serlemitsos, P. J. 1980, *ApJ*, 239, L69